Supercontinuum amplification by Kerr instability

Sagnik Ghosh,[1,*] Nathan G. Drouillard,[2,*] and T. J. Hammond[2,†]
[1]*Department of Electronics and Communication Engineering, Manipal Institute of Technology, Udupi-Karkala Road, Eshwar Nagar, Manipal, Karnataka 576104, India*
[2]*Department of Physics, University of Windsor, Windsor, ON, Canada N9B 3P4*

(Received 26 April 2023; accepted 8 March 2024; published 5 April 2024)

The versatility of optical parametric amplifiers makes them excellent sources for ultrashort visible and infrared pulses that drive strong-field physics experiments. We extend four-wave optical parametric amplification to the strong-field regime, known as Kerr instability amplification, and experimentally verify the modified noncollinear conditions for optimum amplification. We confirm that Kerr instability amplification can be used to amplify spectra that span nearly an octave in a single beam. We also amplify the near-infrared portion of the spectrum to generate the third harmonic downstream.

DOI: 10.1103/PhysRevA.109.043508

I. INTRODUCTION

Next-generation coherent light sources use nonlinear parametric amplification to generate intense pulses from the visible to the infrared (IR) [1]. These versatile ultrafast sources have a broad range of applications including spectroscopy [2], high-harmonic generation [3], and attosecond (1 as $= 10^{-18}$ s) science [4–6]. These optical parametric amplifiers (OPAs) are often pumped by intense femtosecond (1 fs $= 10^{-15}$ s) pulses, generating widely tunable and broad bandwidth coherent pulses with improved pulse contrast [7–10]. The noninversion symmetry required of the $\chi^{(2)}$ optical nonlinearity and phase-matching conditions limit the selection of possible crystals [11]. However, noncollinear geometries circumvent phase-matching limitations, increasing the amplified bandwidth [12].

The next order nonlinearity $\chi^{(3)}$ has also been investigated to amplify visible and near-infrared (NIR) femtosecond pulses [13–16]. In this case, phase matching is achieved when $2\mathbf{k_p} = \mathbf{k_s} + \mathbf{k_i}$, where $\mathbf{k_{p,s,i}}$ are the wave vectors of the pump, signal, and idler, respectively, which is only achieved in a noncollinear geometry. Amplification of up to two orders of magnitude was observed, with a bandwidth that could span up to 75 nm in the visible [17]. When the amplified signal reaches $\sim$1% of the pump intensity, saturation limits further amplification, resulting in a nondegenerate cascaded four-wave mixing (NDC FWM).

NDC FWM creates a series of high-order beamlets spanning multiple octaves [18]. Although these beamlets propagate in unique directions, spatial dispersion compensation has compressed these pulses to the few-cycle regime [19]. Furthermore, these beamlets have been used as a tunable probe for fs stimulated Raman spectroscopy [20–22].

In the more extreme case, where the amplified seed remains below saturation and the pump intensity is near the damage threshold of the $\chi^{(3)}$ material, Kerr instability amplification (KIA) has been proposed to amplify far-IR and THz pulses from a near-IR pump [23]. It demonstrated over three orders of magnitude amplification with a Gaussian beam profile [24]. One of the authors previously reported experimental amplification of widely tuneable but spectrally limited fs pulses using Kerr instability in $Y_3Al_5O_{12}$ (YAG) [24] and magnesium oxide (MgO) [25]. In the visible and the near-IR, gain as high as 18 mm^{-1} was measured.

In this paper, we confirm the broadband spectrum amplification angle dependence predicted by KIA in MgO [26]. Although saturation and geometric effects limit the experimentally measured amplification to two orders of magnitude, our simulations and calculations show that up to five orders of magnitude amplification are realizable.

II. ANGLE-DEPENDENT AMPLIFICATION

The experimental setup is shown in Fig. 1(a). The 785-nm Ti:sapphire laser output 1 mJ, 110 fs pulses at 1 kHz. A CaF_2 window (not shown) split ≈8% of the *s*-polarized beam to create the seed; the half-wave plate (HWP) and polarizer (Pol.) controlled the seed power to 1μJ, while the iris controlled the beam profile to optimize the supercontinuum generated through the focus ($f_1 = 10$ cm) of 5-mm sapphire. The supercontinuum spectrum spanned from 450 to 1000 nm at 50 dB, measured using four different wavelength selecting filters to optimize the signal across the spectrum (350–650, 600–750, 800–900, and >850 nm, where the overlap ensured continuity in the spectrum), measured with an OceanOptics Flame-S spectrometer. The collimating mirror ($f_c = 10$ cm) refocused the seed beam onto the MgO, with ≈5.2× magnification; M_1 steered the seed beam, where the external seed-pump angle was θ.

A computerized delay stage controlled the pump timing; $f_2 = 50$ cm loosely focused ($w_0 \approx 100$ μm) the pump (pulse

*These authors contributed equally to this work.
†thammond@uwindsor.ca

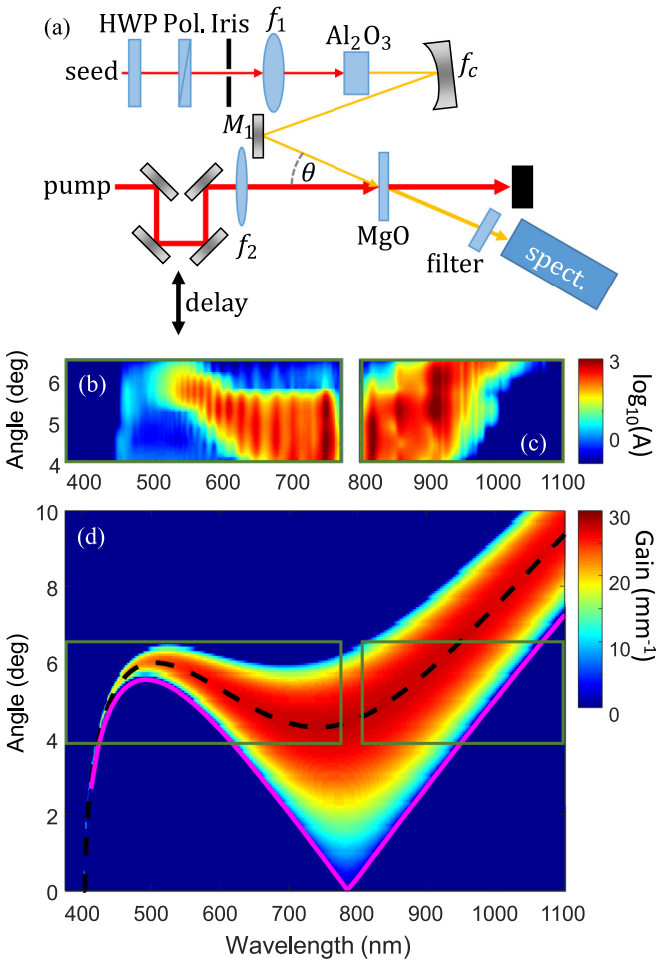

FIG. 1. (a) The setup for supercontinuum amplification. See text for details. Spectral amplification (log colors) measured in the (b) visible and (c) near IR as a function of seed-pump angle. (d) Kerr instability amplification calculation of the gain as a function of relative seed-pump angle and wavelength for a 785-nm pump at $I_0 = 1.5 \times 10^{13}$ W/cm^2. The pink line is the phase-matching condition for FWM, while the black dashed line is maximum gain in KIA. The two green boxes are for the experimentally measured regions, shown in (b) and (c).

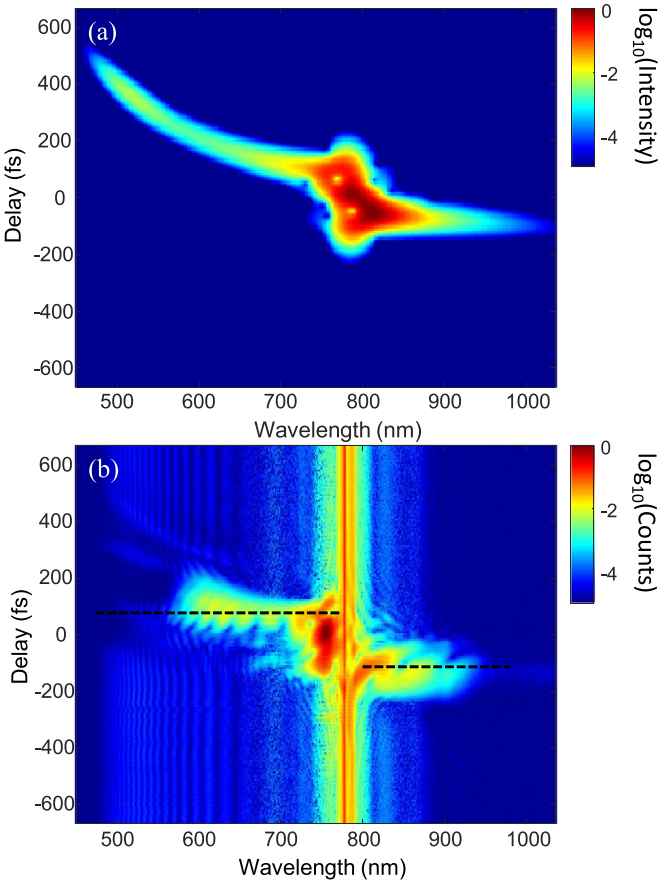

FIG. 2. (a) Temporal evolution of simulated supercontinuum generation matching experimental conditions. (b) Spectral amplification measurement of the supercontinuum seed at 4.9° relative seed-pump angle as a function of pump delay. The amplification process maintains the seed temporal character. Black dashed lines are the regions used to generate the 4.9° contributions in Figs. 1(b) and 1(c).

energy 420 μJ) onto the 0.5-mm MgO crystal. The peak intensity was estimated to be 1.3×10^{13} W/cm^2. Strong-field experiments have shown that MgO can withstand pump intensities up to $I_p = 1.5 \times 10^{13}$ W/cm^2 without damage [25,27–29]. Wavelength and neutral density filters selected the spectrum and intensity for the spectrometer (spect.); the same filters for measuring the seed spectrum were used for the amplified spectra.

We measured amplification in the visible [Fig. 1(b)] and IR [Fig. 1(c)]. The relative seed-pump angles were 4.1°–6.5° with 0.4° steps. Because of the supercontinuum chirp, we show the amplified spectra at a delay exhibiting the maximum amplification [see Fig. 2(b) for further details]. We observed an angle dependence on the amplified bandwidth, at 4.1°, with amplification occurring from 650 to 950 nm. As we increased the relative angle, the amplified bandwidth maximizes near 5°, spanning from 550 to nearly 1000 nm, or nearly an octave. In this region, the transform-limited pulse duration was 5 fs, or two cycles with a central wavelength of 724 nm. Further increasing the angle led to a bifurcation in the amplified spectrum, where the visible portion around 530 nm was amplified, although with decreased gain. At the maximum measured angle, we observed large amplification beyond 1000 nm, measured with an OceanOptics NIRQuest spectrometer.

Saturation limited the maximum amplification to roughly two orders of magnitude. Because we aimed to preserve the generated supercontinuum character for the amplification measurement, we avoided using transmission neutral density (ND) filters to decrease the seed power. We replaced the steering mirror M_1 with BK7 glass to reduce the seed power into the MgO; the seed power was ≈70 nJ. The amplification process saturates when the amplified pulse is ∼1% of the pump intensity [25]. Above saturation, we observed multiple spatially separated beams spanning the UV to the IR, as predicted in NDC FWM [30].

The gain predicted by KIA is shown in Fig. 1(d), where the experimentally measured regions are shown in the green rectangles for comparison. In the limit of low pump intensity,

the angular dependence of the maximum gain predicted by KIA (black dash) is identical to the phase-matching condition of FWM (magenta solid), but at this high-intensity (high-gain) case there is an obvious difference. Near the pump wavelength and longer, the angle for maximum gain KIA is considerably larger than that predicted by FWM. KIA predicts a region of large gain over a broad bandwidth with a small angular dependence, which leads to broadband amplification [26]. The false color scale is the gain predicted by KIA, where near 5° it predicts a region of near uniform amplification spanning 550–1000 nm, in agreement with our experiment.

We simulated the temporal profile of the generated supercontiuum in Fig. 2(a), replicating the experimental parameters. A 120-fs seed pulse focused to 25 μm at 4.5×10^{15} W/cm^2 peak intensity propagated in 5-mm sapphire (see the Appendix for simulation details). We took the windowed Fourier transforms (Gaussian window width 40 fs) of the output pulse to show the temporal character. As the pulse propagated through the focus, the pulse split into a leading IR pulse and a tailing visible pulse [31]. After the focus, the visible portion of the pulse developed a significant chirp due to the material dispersion.

The measured spectrally dependent amplification as a function of pump delay is shown in Fig. 2(b) for 4.9°. Near −100 fs, the IR portion was amplified, while at +100 fs the visible portion was amplified, with an increasing delay for shorter wavelengths. The temporal profile of the amplification is in good agreement with the simulated supercontinuum, demonstrating that KIA maintains the temporal profile of the seed. Black dashed lines represent the regions contributing to Figs. 1(b) and 1(c).

Increasing the angle to 6.5°, we measured the resulting amplified spectra as a function of pump delay in Fig. 3(a). We observed amplification factors ∼three orders of magnitude in the IR. The increased amplification factor was due to the low seed power in this spectral region. Conversely, in the visible, the Kerr instability conditions were not satisfied, which led to a decreased visible signal. Interestingly, the temporal character of the seed was maintained even in this regime. Black dashed lines are the time delays for the lineouts in Fig. 3(b). We show the supercontinuum spectrum (blue) spanning from the visible to the IR that seeds the amplifier. At this angle, we observe amplification around 950 nm, in agreement with the KIA calculation. However, the visible portion decreases by more than an order of magnitude, which is not expected from KIA.

We show all of the amplified spectra that were used to create Figs. 1(b) and 1(c) in Fig. 4. As we increased the angle between the pump and seed, the amplified bandwidth increased. The broadest bandwidth was achieved between 4.9° and 5.3°, in agreement with the KIA calculation.

For larger angles, as shown in Fig. 5, although the amplified long-wavelength portion continues to extend to the IR, there is a discontinuity in the visible. For angles at 6.5° and larger, no visible portion of the spectrum was amplified.

Note that for these images, the color scale denotes the intensity relative to the peak of the spectrum (log scale), whereas in Figs. 1(b) and 1(c), the color scale gives the amplification. The spectral interference in the visible portion is caused by multiple filaments being created in the seed.

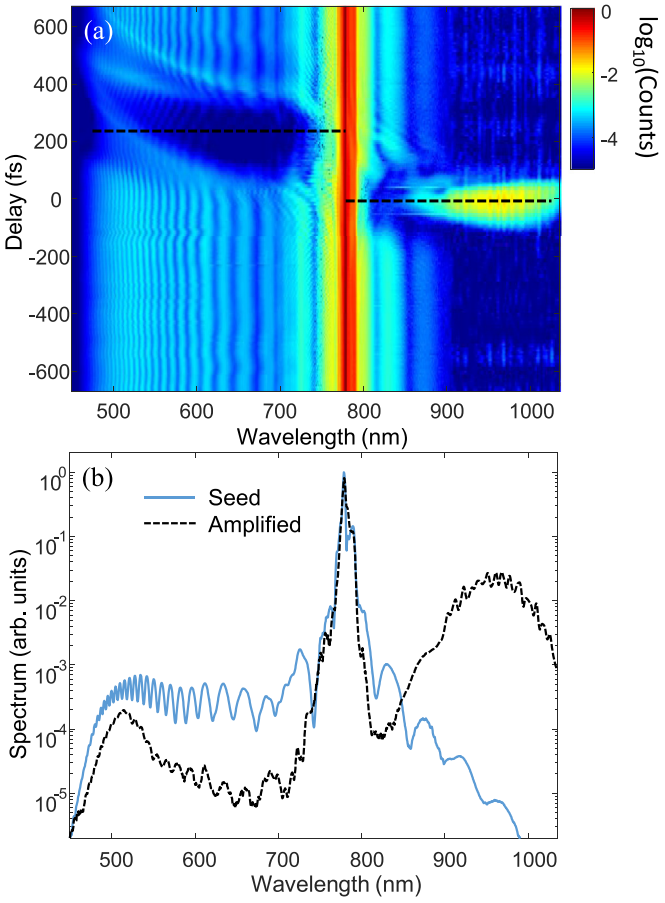

FIG. 3. Spectral amplification measurement of the supercontinuum seed at 6.5° relative seed-pump angle. (a) Amplification occurs only for the IR side of the seed. Black dashed lines are lineouts to generate the spectrum in (b). (b) Supercontinuum seed (blue) and amplified (black dashed) spectra. The wavelength region >900 nm was taken with an IR spectrometer.

We note that the plasma-induced index change, $\Delta n_{\mathrm{pl}} = -\omega_{\mathrm{pl}}^2/\omega_p^2$, where $\omega_{\mathrm{pl}}^2 = \frac{N_e e^2}{\epsilon_0 m^*}$ (N_e is the electron density, e is the fundamental unit of charge, ϵ_0 is the permittivity of free space, and m^* is the effective electron mass) is the plasma frequency, is comparable to the Kerr-induced index change, $\Delta n_{\mathrm{Kerr}} = n_2 I_p$, at these intensities [32]. However, because the sign of Δn_{pl} is the opposite of Δn_{Kerr}, plasma may both help and hinder the amplification. With such a tight focus to create these intensities, self-focusing limits the crystal thickness, and the plasma-induced index change may improve pump pulse propagation in the nonlinear medium. However, it may also limit the amplification efficiency by decreasing the modulation instability. Further investigation of these competing processes is necessary, but beyond the scope of this work.

III. BROADBAND AMPLIFICATION

Although NDC FWM exploits the Kerr response to generate a multioctave spanning spectrum [19], it produces a series of beamlets with each beamlet containing only a fraction of the total spectral bandwidth. Conversely, KIA can amplify broadband spectra that support few-cycle pulses in a single

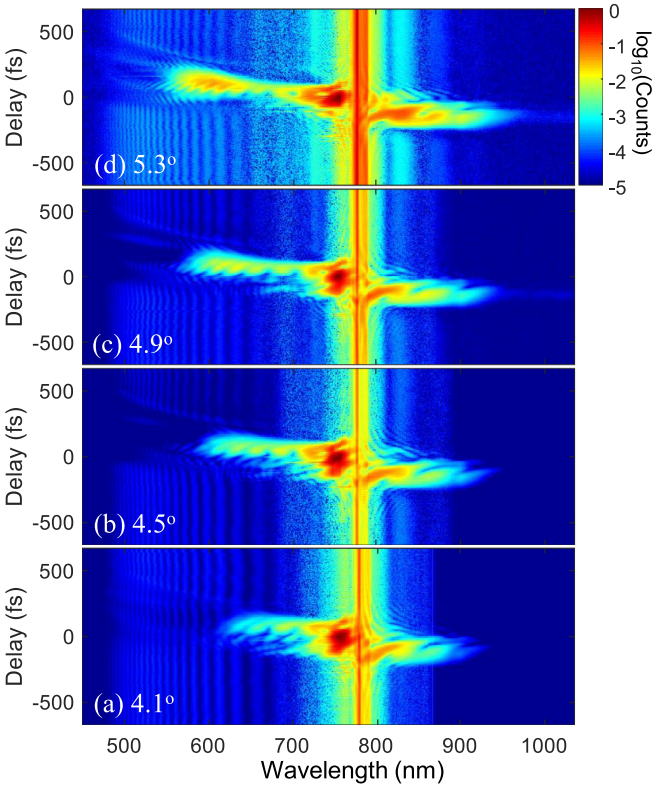

FIG. 4. Spectral amplification measurement of the supercontinuum seed from 4.1° to 5.3° as a function of delay. As the pump-seed angles (given in figures) increased, the amplified bandwidth increases.

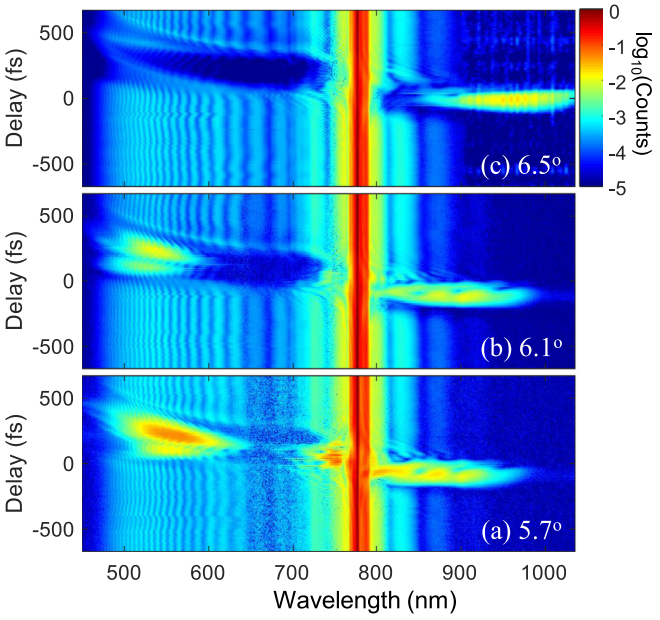

FIG. 5. Spectral amplification measurement of the supercontinuum seed from 5.7° to 6.5° as a function of delay. For these larger angles, there was a discontinuity in the amplification. At 6.5°, there was no amplification in the visible.

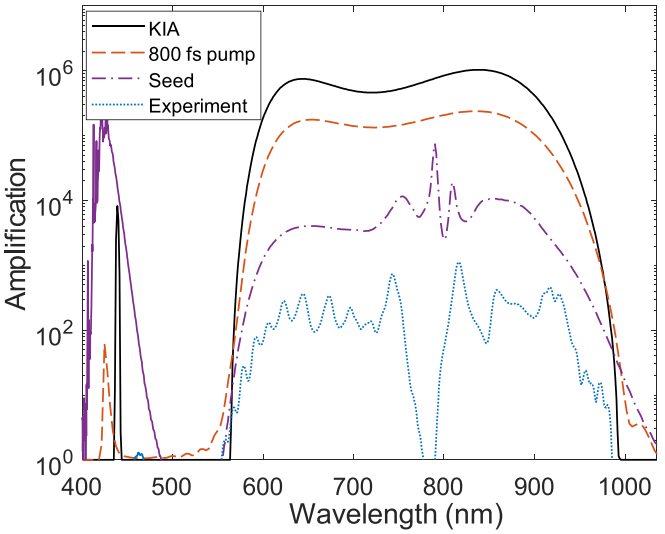

FIG. 6. Simulation and experimental amplification at 4.9°. The KIA calculation (black solid lline) agrees well with the two-dimensional (2D) simulation (orange dashed line); the amplification difference comes from KIA not accounting for the creation of an idler field. The spatial profile reduced the amplification of the transform-limited supercontinuum seed pulse when the seed and pump beam waists were the same (purple dotted-dashed line); the large gain in the blue end of the spectrum is because there was a negligible seed spectrum in this region. The bandwidth of the experimentally measured amplified spectrum (blue dotted line) is in good agreement with theory.

beam, as shown in Fig. 6. In these simulations and experiment, we observed the output at 4.9°. The KIA calculation (black) predicts a broadband amplification of nearly six orders of magnitude, with a full width at half maximum (FWHM) spanning from 600 to 900 nm. This amplification corresponds to a gain of $g = 27\ \mathrm{mm}^{-1}$, with the transform-limited pulse duration being 4.7 fs and a central wavelength of 714 nm, supporting a two-cycle pulse. We simulated the nonlinear propagation of the FWM process by seeding with a broadband seed (red). The simulation used the experimental parameters, but the pump pulse character was modified to 800 fs in duration and a minimum waist of $w_p = 250$ μm to avoid self-phase modulation and self-focusing effects of the pump, approximating the plane-wave long-pump limit of KIA. The difference in the amplification stems from the KIA result that amplification $A = \exp(gz)$, where z is the propagation distance, whereas from FWM $A = \cosh^2(gz/2)$ [26].

We compare this broadband amplification to the amplification of the simulated seed previously discussed in Fig. 2(a) (purple dotted-dashed line). In this case, the seed duration transform limit was 10 fs, while the seed waist matched the pump waist, $w_s = w_p$, and the pump pulse duration was 100 fs, matching experimental conditions. The seed profile and the shorter pump duration decreased the amplification relative to the maximum possible amount. We also show the experimentally realized amplification (blue dotted line). The bandwidth of the amplified spectrum agrees well with theory, but the maximum amplification is significantly decreased from the theoretical value because of saturation. To

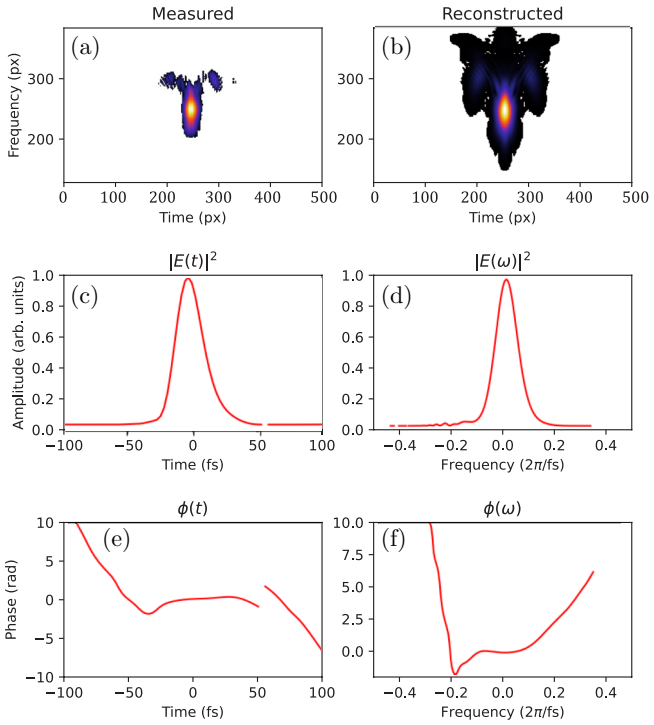

FIG. 7. Characterizing the NIR portion of the amplified spectra. (a) The measured and (b) reconstructed spectrogram after 500 iterations, with an error of 1.01. (c) The pulse intensity measured duration was 24 fs; compensating for the dispersion (e) predicts a 20 fs pulse. (d) Spectral amplitude and (f) phase are also presented.

measure the amplification factor, we smoothed the seed spectrum to reduce its oscillation amplitude. We note that there was little amplification near the seed central wavelength in this configuration.

IV. NONLINEAR OPTICS WITH AMPLIFIED BEAM

We demonstrate that these amplified pulses can be a source for ultrashort nonlinear processes by generating the third harmonic. Using the setup of Fig. 1 with a pump-seed angle of 5.7° led to large amplification around 900 nm. We chose this portion of the spectrum to generate the third harmonic because the NIR side of the supercontinuum seed exhibited less chirp than the visible portion of the spectrum, as shown in Fig. 2(a). At the maximum amplification, near zero delay, we measured a FWHM bandwidth of 83 nm, with a transform-limited pulse duration of 15 fs. A home-built frequency-resolved optical gating (FROG) measurement returned a 24 fs pulse (20 fs for optimally compressed) with a central wavelength at 880 nm, consistent with the spectrum, as shown in Fig. 7. Figure 7 shows the measured and reconstructed FROG traces, where the error in the reconstruction is 1.01. With an 800-nm long-pass filter, we measured the amplified pulse energy of 0.54 μJ, yielding a peak power of 23 MW. This amplified beam peak power is consistent with previous measurements of 0.5% of the pump.

We focused this beam ($f = 75$ mm) onto another 0.5-mm-thick MgO crystal to generate the third harmonic, and passed

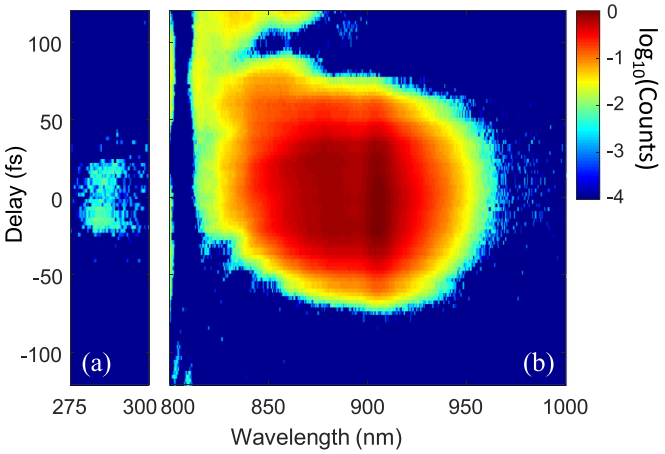

FIG. 8. Third-harmonic generation from amplified NIR spectrum. (a) The third harmonic, centered at 287 nm, was only created when the NIR portion is strongly amplified. The short coherence length, $L_{\mathrm{coh}} \approx 3$ μm, limited the third-harmonic efficiency. (b) The FWHM bandwidth of the NIR spectrum was 83 nm, with a transform-limited pulse duration of 15 fs.

the resulting beam through a 282-nm filter before the spectrometer. Although phase matching ($L_{\mathrm{coh}} \approx 3$ μm) severely limited the conversion efficiency, we were able to detect the third harmonic at 287 nm when the near-IR portion of the supercontinuum was amplified, as shown in Fig. 8. At the estimated intensity $>10^{12}$ W/cm^2, third-harmonic generation in MgO has been shown to be nonperturbative [33], leading the way to further high-harmonic generation studies in condensed matter.

We expect that KIA could be a route to creating a simplified amplifier for few-cycle pulses directly from a laser oscillator. By spectrally broadening the output of a mode-locked laser in dispersion controlled fibers [34,35], KIA could amplify these pulses by many orders of magnitude without external pulse selection. This broadband amplification will be an asset for developing compact few-cycle sources, and may be useful as an initial amplification stage in broadband optical parametric amplifiers [36,37].

V. CONCLUSIONS

In conclusion, we have observed amplification of a supercontinuum spectrum from 500 nm to over 1 μm in a single beam. The amplification bandwidth depends on the relative pump-seed angle, in agreement with KIA theory. Although KIA theory predicts amplification factors $>10^5$, we only observed amplification of two to three orders of magnitude, limited by geometrical effects and saturation. We observed that the amplification process did not significantly change the temporal nature of the seed; we expect that chirping the seed could allow for further amplification by reducing the peak power during amplification. We demonstrated that these amplified pulses can be a source for nonlinear optics by generating the third harmonic, leading the way for future ultrashort nonlinear experiments.

ACKNOWLEDGMENTS

S.G. acknowledges funding from Mitacs Globalink Research Internship. We acknowledge funding from Natural Sciences and Engineering Research Council of Canada (RGPIN-2019-06877) and the University of Windsor Xcelerate grant (No. 5218522). T.J.H. thanks Giulio Vampa, Thomas Brabec, and Claire Duncan for useful conversations.

APPENDIX: SIMULATIONS

We use the forward Maxwell's equation (FME) to simulate the Kerr instability amplification (KIA) and the seed supercontinuum [38,39]:

$$\frac{\partial}{\partial z}E(\mathbf{r},\omega) = i\frac{c}{2n(\omega)\omega}\nabla_\perp^2 E(\mathbf{r},\omega) + i\frac{\omega}{c}[n(\omega)-n_g]E(\mathbf{r},\omega) + i\frac{\mu_0\omega c}{2n(\omega)}P_{\mathrm{NL}}(\mathbf{r},\omega). \tag{A1}$$

We solve Eq. (A1) by fourth-order Runge-Kutta integration in the frequency domain. For modeling the amplification, we simulate the propagation in two dimensions, where $\nabla_\perp^2 = \frac{\partial^2}{\partial x^2}$ is the transverse coordinate. To calculate the spatial dispersion [first term in Eq. (A1)], we use the fast Fourier transform to propagate the field in the momentum domain, and then inverse fast Fourier transform back to the spatial domain for the nonlinear and temporal dispersion calculations [40]. Further details of the simulation can be found in Ref. [26].

To generate the seed, as shown in Fig. 2(a), we exploit the cylindrical symmetry, that is $\nabla_\perp^2 = \frac{1}{\rho}\frac{\partial}{\partial\rho}(\rho\frac{\partial}{\partial\rho})$, which requires a Hankel transform [41]. We vary the beam focus within the sapphire to match the experimentally measured spectrum. We found that a one-dimensional (1D+time) simulation did not predict the pulse splitting that we experimentally measured. Conversely, both 2D (propagation and transverse spatial)+time and cylindrical symmetry cases exhibited pulse splitting, with spectral features changing due to varying focus, propagation, and intensity.

We only account for the $\chi^{(3)}$ nonlinear polarizability, $P_{\mathrm{NL}} = \epsilon_0\chi^{(3)}E^3$. We assume a wavelength- (and time-) independent nonlinear index of refraction of $n_2 = 3\chi^{(3)}/(4\epsilon_0 c n_p^2)$, where n_p is the index at the pump wavelength. We use the values of $n_2 = 4\times10^{-16}$ cm^2/W [42] for MgO and $n_2 = 2.8\times10^{-16}$ cm^2/W [43] for sapphire ordinary axis; we do not account for plasma effects in our model. We account for the linear index of refraction of the material $n(\omega)$ [44,45], which includes higher orders of dispersion.

To compare the KIA result to the simulation, we initiate the model in the momentum-frequency domain. We find that beginning in the Fourier domain reduces the background noise, which is key when simulating the high gain. To simulate the broadband case, as shown in Fig. 6 (red), the seed field is $E_s(\omega,k) = 10^{-8}E_p$ for $\omega > 0$ and $k > 0$ and 0 otherwise, where E_p is the peak pump field strength. This weak seed field strength allows for large gain over 0.5-mm-thick MgO without saturation effects.

[1] H. Fattahi, H. G. Barros, M. Gorjan, T. Nubbemeyer, B. Alsaif, C. Y. Teisset, M. Schultze, S. Prinz, M. Haefner, M. Ueffing, A. Alismail, L. Vámos, A. Schwarz, O. Pronin, J. Brons, X. T. Geng, G. Arisholm, M. Ciappina, V. S. Yakovlev, D. E. Kim *et al.*, Third-generation femtosecond technology, Optica **1**, 45 (2014).

[2] J. Biegert, P. K. Bates, and O. Chalus, New mid-infrared light sources, IEEE J. Sel. Top. Quantum Electron. **18**, 531 (2012).

[3] A. Shiner, B. Schmidt, C. Trallero-Herrero, H. Wörner, S. Patchkovskii, P. Corkum, J.-C. Kieffer, F. Légaré, and D. Villeneuve, Probing collective multi-electron dynamics in xenon with high-harmonic spectroscopy, Nat. Phys. **7**, 464 (2011).

[4] G. Vampa, T. J. Hammond, N. Thiré, B. Schmidt, F. Légaré, C. McDonald, T. Brabec, and P. Corkum, Linking high harmonics from gases and solids, Nature (London) **522**, 462 (2015).

[5] T. J. Hammond, S. Monchocé, C. Zhang, G. Vampa, D. Klug, A. Y. Naumov, D. M. Villeneuve, and P. B. Corkum, Integrating solids and gases for attosecond pulse generation, Nat. Photon. **11**, 594 (2017).

[6] K. Zinchenko, F. Ardana-Lamas, I. Seidu, S. Neville, J. van der Veen, V. Lanfaloni, M. Schuurman, and H. Wörner, Sub-7-femtosecond conical-intersection dynamics probed at the carbon K-edge, Science **371**, 489 (2021).

[7] T. Kobayashi, J. Liu, and K. Okamura, Applications of parametric processes to high-quality multicolour ultrashort pulses, pulse cleaning and CEP stable sub-3 fs pulse, J. Phys. B: At. Mol. Opt. Phys. **45**, 074005 (2012).

[8] F. Wagner, C. P. João, J. Fils, T. Gottschall, J. Hein, J. Körner, J. Limpert, M. Roth, T. Stöhlker, and V. Bagnoud, Temporal contrast control at the PHELIX petawatt laser facility by means of tunable sub-picosecond optical parametric amplification, Appl. Phys. B **116**, 429 (2014).

[9] C. Dorrer, A. Conentino, D. Irwin, J. Qiao, and J. Zuegel, OPCPA front end and contrast optimization for the OMEGA EP kilojoule, picosecond laser, J. Opt. **17**, 094007 (2015).

[10] M. Sun, X. Xie, J. Zhu, X. Zhang, Y. Zhang, P. Zhu, A. Guo, J. Kang, H. Zhu, Q. Yang, and X. Liang, Experimental demonstration of 10^{11} temporal contrast in pure nanosecond optical parametric chirped pulse amplifiers, Appl. Opt. **60**, 2056 (2021).

[11] C. Manzoni and G. Cerullo, Design criteria for ultrafast optical parametric amplifiers, J. Opt. **18**, 103501 (2016).

[12] G. Cerullo and S. D. Silvestri, Ultrafast optical parametric amplifiers, Rev. Sci. Instrum. **74**, 1 (2003).

[13] J. Hansryd, P. A. Andrekson, M. Westlund, J. Li, and P.-O. Hedekvist, Fiber-based optical parametric amplifiers and their applications, IEEE J. Sel. Top. Quantum Electron. **8**, 506 (2002).

[14] A. Dubietis, G. Tamošauskas, P. Polesana, G. Valiulis, H. Valtna, D. Faccio, P. D. Trapani, and A. Piskarskas, Highly

efficient four-wave parametric amplification in transparent bulk Kerr medium, Opt. Express **15**, 11126 (2007).
[15] H. Valtna, G. Tamošauskas, A. Dubietis, and A. Piskarskas, High-energy broadband four-wave optical parametric amplification in bulk fused silica, Opt. Lett. **33**, 971 (2008).
[16] S. Huang, P. Wang, X. Shen, and J. Liu, Broadband ultrashort light generation from a narrowband seed, Opt. Laser Technol. **145**, 107489 (2022).
[17] A. Dubietis, G. Tamošauskas, G. Valiulis, and A. Piskarskas, Ultrafast four-wave optical parametric amplification in transparent condensed bulk media, Laser Chem. **2008**, 534951 (2008).
[18] H. Crespo, J. Mendonça, and A. D. Santos, Cascaded highly nondegenerate four-wave-mixing phenomenon in transparent isotropic condensed media, Opt. Lett. **25**, 829 (2000).
[19] R. Weigand, J. T. Mendonça, and H. M. Crespo, Cascaded nondegenerate four-wave-mixing technique for high-power single-cycle pulse synthesis in the visible and ultraviolet ranges, Phys. Rev. A **79**, 063838 (2009).
[20] L. Zhu, W. Liu, and C. Fang, Tunable sideband laser from cascaded four-wave mixing in thin glass for ultra-broadband femtosecond stimulated Raman spectroscopy, Appl. Phys. Lett. **103**, 061110 (2013).
[21] L. Zhu, W. Liu, and C. Fang, A versatile femtosecond stimulated Raman spectroscopy setup with tunable pulses in the visible to near infrared, Appl. Phys. Lett. **105**, 041106 (2014).
[22] D. Dietze and R. Mathies, Femtosecond stimulated Raman spectroscopy, ChemPhysChem **17**, 1224 (2016).
[23] M. Nesrallah, G. Vampa, G. Bart, P. B. Corkum, C. R. McDonald, and T. Brabec, Theory of Kerr instability amplification, Optica **5**, 271 (2018).
[24] G. Vampa, T. J. Hammond, M. Nesrallah, A. Y. Naumov, P. B. Corkum, and T. Brabec, Light amplification by seeded Kerr instability, Science **359**, 673 (2018).
[25] C. Jayalath Arachchige, J. A. Stephen, and T. J. Hammond, Amplification of femtosecond pulses based on $\chi^{(3)}$ nonlinear susceptibility in MgO, Opt. Lett. **46**, 5521 (2021).
[26] S. Ghosh, N. G. Drouillard, and T. J. Hammond, Single-stage few-cycle pulse amplification, Phys. Rev. A **109**, 013511 (2024).
[27] Y. S. You, D. A. Reis, and S. Ghimire, Anisotropic high-harmonic generation in bulk crystals, Nat. Phys. **13**, 345 (2017).
[28] A. Korobenko, T. J. Hammond, C. Zhang, A. Y. Naumov, D. M. Villeneuve, and P. B. Corkum, High-harmonic generation in solids driven by counter-propagating pulses, Opt. Express **27**, 32630 (2019).
[29] D. H. Ko, G. G. Brown, C. Zhang, and P. B. Corkum, Delay measurements of attosecond emission in solids, J. Phys. B: At. Mol. Opt. Phys. **53**, 124001 (2020).
[30] R. Weigand and H. M. Crespo, Fundamentals of highly nondegenerate cascaded four-wave mixing, Appl. Sci **5**, 485 (2015).
[31] A. Dubietis, G. Tamošauskas, R. Šuminas, V. Jukna, and A. Couairon, Ultrafast supercontinuum generation in bulk condensed media, Lith. J. Phys. **57**, 113 (2017).
[32] S. Xu, T. Jia, H. Sun, C. Li, X. Li, D. Feng, J. Qiu, and Z. Xu, Mechanisms of femtosecond laser-induced breakdown and damage in MgO, Opt. Commun. **259**, 274 (2006).
[33] M. Hussain, F. Lima, W. Boutu, H. Merdji, M. Fajardo, and G. O. Williams, Demonstration of nonperturbative and perturbative third-harmonic generation in MgO by altering the electronic structure, Phys. Rev. A **105**, 053103 (2022).
[34] W. H. Reeves, D. V. Skryabin, F. Biancalana, J. C. Knight, P. S. J. Russell, F. G. Omenetto, A. Efimov, and A. J. Taylor, Transformation and control of ultrashort pulses in dispersion-engineered photonic crystal fibres, Nature (London) **424**, 511 (2003).
[35] C. Markos, J. C. Travers, A. Abdolvand, B. J. Eggleton, and O. Bang, Hybrid photonic-crystal fiber, Rev. Mod. Phys. **89**, 045003 (2017).
[36] B. Schmidt, N. Thiré, M. Boivin, A. Laramée, F. Poitras, G. Lebrun, T. Ozaki, H. Ibrahim, and F. Légaré, Frequency domain optical parametric amplification, Nat. Commun. **5**, 3643 (2014).
[37] L. Xu and E. J. Takahashi, Dual-chirped optical parametric amplification of high-energy single-cycle laser pulses, Nat. Photon. **18**, 99 (2024).
[38] A. V. Husakou and J. Herrmann, Supercontinuum generation of higher-order solitons by fission in photonic crystal fibers, Phys. Rev. Lett. **87**, 203901 (2001).
[39] L. Bergé, J. Rolle, and C. Köhler, Enhanced self-compression of mid-infrared laser filaments in argon, Phys. Rev. A **88**, 023816 (2013).
[40] G. P. Agrawal, in *Nonlinear Fiber Optics* (Academic Press, Oxford, 2013).
[41] A. Wyatt, Hankel transform, https://www.mathworks.com/matlabcentral/fileexchange/15623-hankel-transform (2009), accessed 13 January 2023.
[42] R. Adair, L. L. Chase, and S. A. Payne, Nonlinear refractive index of optical crystals, Phys. Rev. B **39**, 3337 (1989).
[43] A. Major, F. Yoshino, I. Nikolakakos, J. Aitchison, and P. Smith, Dispersion of the nonlinear refractive index in sapphire, Opt. Lett. **29**, 602 (2004).
[44] R. Stephens and I. Malitson, Index of refraction of magnesium oxide, J. Res. Natl. Bur. Stand. **49**, 249 (1952).
[45] I. Malitson, Refraction and dispersion of synthetic sapphire, J. Opt. Soc. Am. **52**, 1377 (1962).